

Foreign Body Detection in Frozen Food by Dual Energy X-Ray Transmission

* **Christine BAUER, Rebecca WAGNER and Johannes LEISNER**

Fraunhofer IIS, Fraunhofer Institute for Integrated Circuits IIS, Division Development Center X-Ray Technology, Flugplatzstr, 75, 90768 Fürth, Germany
Tel.: +49911580617663, fax: +49911580617299
E-mail: christine.bauer@iis.fraunhofer.de

Received: 22 October 2021 /Accepted: 23 November 2021 /Published: 30 November 2021

Abstract: Foreign bodies of different types may find their way unnoticed into frozen food during processing or while packing. These contaminating objects show a great variety of materials, but consist most likely of glass, plastics, metal or (fish-) bone. The contaminants may cause considerable product recalls because of their hazardous nature for the consumer, leading to suffocation or shortness of breath. Eventually, the reputation of the respective manufacturer is long-termed harmed. Dual energy X-ray transmission is a powerful tool in non-destructive testing and thus may provide a solution to detect different foreign bodies in frozen food. We used this method for studying different frozen foods like mixed berries or vegetables and convenience food contaminated with aluminum, synthetic bones, Teflon, steel and glass test objects of different diameters in the range from 0.3 mm to 10 mm. The study shows that dual energy X-ray transmission is suitable to detect certain contaminants in frozen food while it reveals weakness in reliably discovering plastics. A general limitation of a contaminants' size that can be detected with this method is the spatial resolution of the measurement setup. Especially in highly heterogeneous environments, dual energy outperforms conventional X-ray transmission.

Keywords: Dual energy, X-ray, X-ray transmission, Basis material decomposition, Food safety, Food contaminants, Foreign body detection.

1. Introduction

Today many producers have to call back their products due to appearing safety issues or product defects. On the German market, the number of product recalls increases every year (except in 2017) resulting in a record high of 297 in 2019 (Fig. 1) [1].

In that year, almost one third of the product recalls, namely 90, occurred in the food sector followed by defective toys and faulty leisure items or sporting goods (Fig. 2).

The main reasons for the food producers to recall their products are faulty packaging and foreign bodies, which entered the product prior to packaging. The

product recalls are mainly triggered by incidences of suffocation or shortness of breath (40 %) [1].

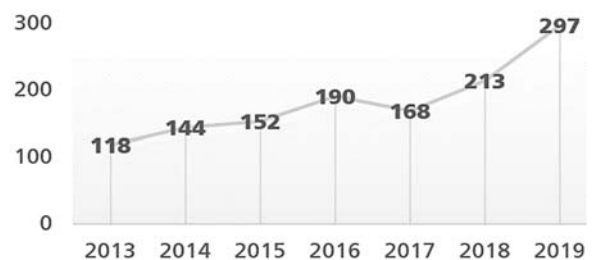


Fig. 1. Number of published product recalls on the German market from 2013 to 2019 (data from [1]).

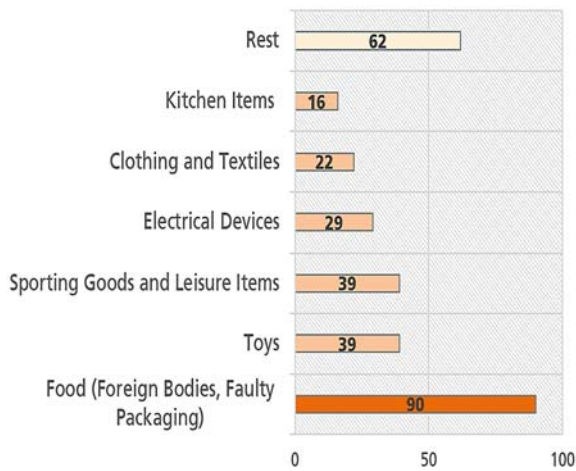


Fig. 2. Number of product recalls per product group on the German market in 2019 (data from [1]).

It can be said that product recalls are not only very costly (around \$ 10⁶ for a company [2]), but also lead to the elimination of high amounts of goods (e.g. food, electronic devices) and a long-lasting harm of the manufacturer's reputation.

There are various technologies to find foreign bodies in products. Optical methods are limited to the objects' surface, while others rely on electrical conductivity or magnetism [3]. In comparison to technologies like metal detection, X-ray transmission (XRT) is not limited to one kind of material and may find foreign bodies like plastics, glass, bone fragments and metals also in packed food [4]. Additionally, there are also several approaches to detect defects in fruits with X-ray imaging [5, 6].

Nevertheless, XRT has its limits, as objects with low attenuation are hard to find especially in heterogeneous environments, i.e. environments that lead to a considerable spatial fluctuation of X-ray attenuation. An approach that is used not only in modern medicine but also in various security applications and non-destructive testing (NDT) is the use of dual energy methods [7]. They are based on the material specific variation in transmission and absorption of X-rays with energy. Unlike standard XRT that only allows separating materials based on their X-ray attenuation, dual energy X-ray transmission (DE-XRT) is capable of acquiring quantitative information like the areal density [8] or the mass percentage of measured materials [9]. Thereby the areal density image of one material is mostly independent of the other material.

Applications which need an NDT technology for quality control and involve highly heterogeneous 'background material' like food are prone to be solved with a DE-XRT approach. In this paper, we present several examples for the detection of foreign bodies in food using DE-XRT. While we will concentrate on frozen food for the remainder of this publication, the method was also successfully applied to food types like nuts, wafer treats and tofu balls [10].

2. Experimental

2.1. Sample Materials

In total, five samples were chosen to test various types of frozen food including convenience food. The studied samples were:

- A frozen paella, a rice dish with vegetables, seafood, salmon and chicken,
- Whole frozen strawberries,
- A frozen berry mix containing strawberries, blackberries, raspberries, redcurrants, blueberries and sour cherries,
- Frozen Asian styled fried vegetables with cauliflower, savoy, carrots, onion, pepper, ginger and soy sauce,
- Frozen buttered vegetables, namely peas, carrots, corn and cauliflower.

Eight test cards including five calibrated spherical test objects of different diameters d made by RONDOTEST® [11] were used (Table 1, Fig. 3 right), namely aluminum, glass, steel (AISI 304) and Teflon (PTFE). Two additional test cards contained cubic test bodies of synthetic bone with edge length d (Table 1, Fig. 3 left).

Table 1. Used test cards with their respective materials and thicknesses.

Material	Thickness [mm]				
	d ₁	d ₂	d ₃	d ₄	d ₅
Aluminum	0.5	0.8	1.0	1.2	1.5
Aluminum	2.0	2.5	3.0	3.5	4.0
Synth. Bone	2.0	3.0	4.0	5.0	6.0
Synth. Bone	6.0	7.0	8.0	9.0	10.0
Glass	0.5	0.8	1.0	1.2	1.5
Glass	1.5	2.0	2.5	3.0	3.5
Steel AISI304	0.3	0.4	0.5	0.6	0.8
Steel AISI304	0.6	0.8	1.0	1.2	1.5
Teflon PTFE	2.0	2.5	3.0	3.5	4.0
Teflon PTFE	4.0	5.0	6.0	7.0	8.0



Fig. 3. Left: Test card for synthetic bone with five cubic test bodies (6 mm to 10 mm). Right: Test card for glass with five spherical test bodies (1.5 mm to 3.5 mm).

2.2. Dual Energy X-ray Transmission

The measurements were performed using a drawer system moving between a high-power X-ray source (Comet MXR225/HP11) as well as a dual energy line detector (Fig. 4). The used detector was a Hamamatsu C10800-09FCM-C with a pixel pitch of 0.4 mm. As

the detector was placed directly below the drawer, the X-ray images are obtained with minimal magnification. Therefore, the pixel pitch of the detector corresponds directly to the spatial resolution of the images. The detector consists of two sensor layers, so that it records two images (high- and low-energy) simultaneously at different X-ray energies. The samples were placed in the drawer, which moved with a speed of approx. 170 mm/s. The scans were carried out with 100 kV, 5 mA and an exposure time of 2.67 ms per recorded line.

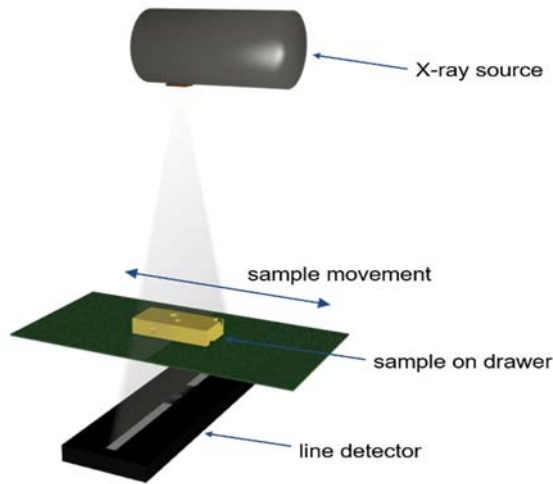


Fig. 4. Scheme of the measurement procedure: the sample is moved between the X-ray source and the dual energy line detector (adapted from [12] published under license CC BY 4.0).

For analysis of the data, basis material decomposition (BMD) was applied [8, 9, 13]. This method utilizes the energy dependence of X-ray attenuation. It requires two images of a sample, recorded with different spectral parameters, i.e. one with lower energy (LE) and one with higher energy (HE). This can be achieved by different means. For the work presented in this paper, a dual energy detector was used. Other options would be the use of different filters or changing the tube voltage. Applying BMD to two spectrally different XRT images, yields the areal densities p_l and p_h of two materials l (light) and h (heavy) that have to be chosen by the user. The areal density is defined as the materials density multiplied by its thickness [12] (Fig. 5).

BMD is based on the Lambert-Beer law, which describes the intensity I behind an object with areal density p and mass attenuation coefficient μ' :

$$I = I_0 e^{-p\mu'}, \quad (1)$$

where I_0 is the non-attenuated intensity.

This approach includes the attenuation of X-rays by Compton scattering as well as photoelectric absorption. Typical laboratory X-ray sources are not monochromatic. Thus, the detected non-attenuated intensity is given by:

$$I_0 = \int dE S(E) * D(E), \quad (2)$$

with $D(E)$ being the detector efficiency and $S(E)$ the spectrum emitted by the source. Using Eq. 1 and Eq. 2 leads to:

$$I = \int dE * e^{-p\mu'(E)} * S(E) * D(E) \quad (3)$$

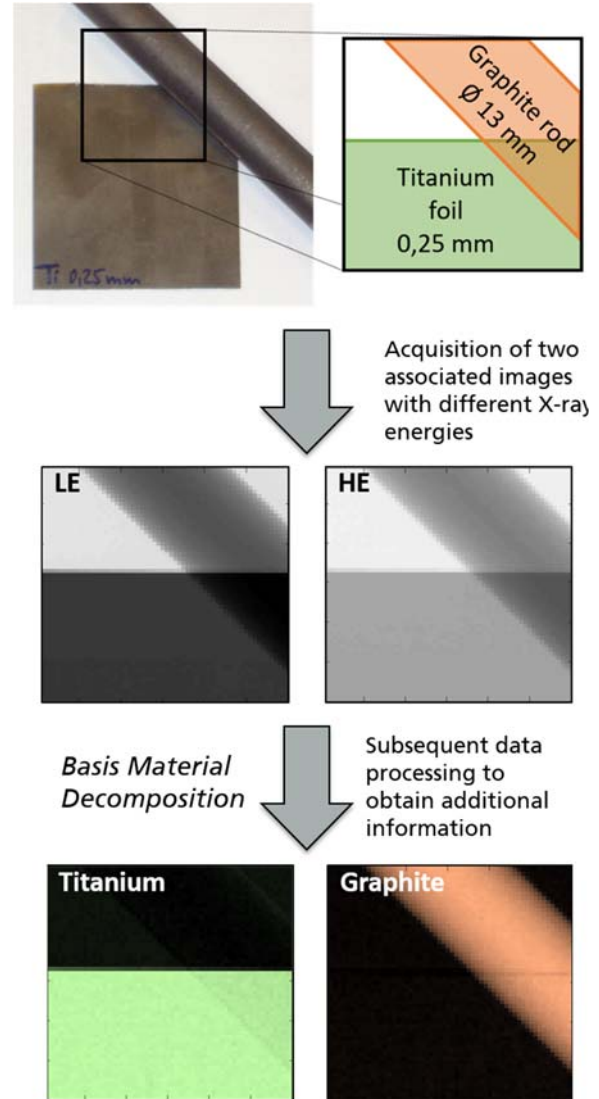


Fig. 5. Scheme of the data processing procedure exemplified with two pure materials: a graphite rod overlapping a titanium foil (adapted from [14]).

The attenuation coefficients of different materials sum up when more than one material is penetrated. Acquiring two measurements at different spectral parameters leads to a set of two equations. This set describes the extinction of the same material composition at different spectral parameters k , leading to:

$$I_k = \int dE * e^{-\sum p_j \mu'_j(E)} * S_k(E) * D(E) \quad (4)$$

with j being the index of the material. To solve this set of equations, the product $D(E) * S(E)$ has to be known.

It can be obtained either by simulation or measurement techniques [15]. As the mass attenuation coefficient μ' is tabulated, equation (4) allows to compute the areal densities p_1 and p_2 of two chosen materials by solving the set of equations given by two measurements with different X-ray energies.

The investigated samples, especially the food, are chemically complex materials, so their X-ray attenuation properties are determined by their effective atomic number Z_{eff} . It can be calculated by using

$$Z_{eff}^k = \frac{\sum_i Z_i^k \rho_i}{\sum_i \rho_i}, \text{ with } k \approx 3, \quad (5)$$

where Z_i are the constituent's atomic numbers and ρ_i the constituents' partial chemical densities [16].

Here, the light material was the background, i.e. the food with an assumed effective atomic number around 7.5 that was adjusted to the respective object (for details see 3. Results). The heavy material was aluminum (effective atomic number of 13), glass ($Z_{eff} = 11.6$), PTFE ($Z_{eff} = 10$), steel ($Z_{eff} = 26$) or bone ($Z_{eff} = 11.3$).

3. Results

Fig. 6 shows the high-energy image of the frozen Asian styled fried vegetables including the ten aluminum test objects. The five aluminum beads of the first card with a diameter between 2.0 mm and 4.0 mm are difficult to see with the bare eye and can hardly be discriminated from the food. The beads of the second card with smaller diameter (0.5 mm to 1.5 mm) are completely unrecognizable.

In this case, detection by automated image processing would be very challenging. The overlapping diverse vegetables create a highly heterogeneous absorption image that is almost impossible to be segmented, especially with automatic thresholding methods.

The resulting BMD image for aluminum is shown in Fig. 7. It displays the areal density of aluminum. The frozen vegetables ($Z_{eff} = 7.7$) vanish almost completely in this image and some of the test bodies can clearly be seen. Here, the segmentation of the aluminum beads is feasible for the bigger spheres (2.0 mm to 4.0 mm). For the smaller beads only 1.0, 1.2 and 1.5 mm can be detected.

With a line tracker of five pixels in width (Fig. 8) the grey value in the HE X-ray projection and the areal density of the test bodies were obtained (Fig. 9 for the bigger spheres and Fig. 10 for the smaller beads).

The line profiles show fluctuations of the grey values due to the heterogeneous structure of the food. As a result, even the bigger test bodies can hardly be identified based on their grey values. However, the areal density line profiles show that there is sufficient contrast between background and several of the test

bodies. Of the five bigger beads (Fig. 9), four could be identified by applying a threshold, while the smallest one with $d = 2$ mm is harder to distinguish from noise.

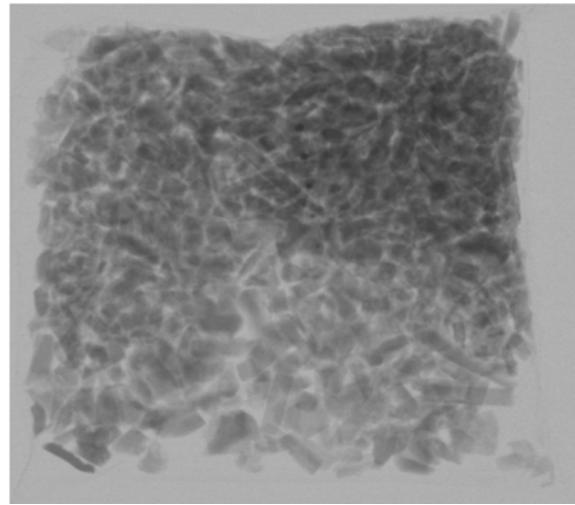


Fig. 6. High-energy XRT image of frozen Asian styled fried vegetables contaminated with aluminum.

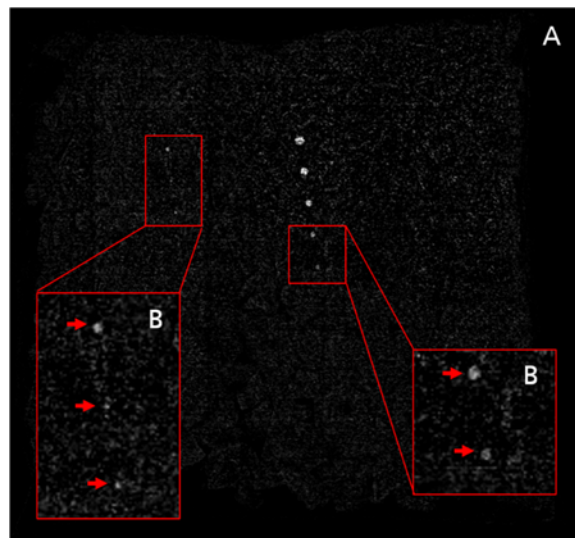


Fig. 7. A: Areal density image of aluminum. The five bigger contaminants are clearly visible, while only three of the smaller ones can be detected. The frozen vegetables ('background') disappear. B: Magnification of 2.5 of the framed areas in A (red). Red arrows indicate the approximate location of the aluminum beads.

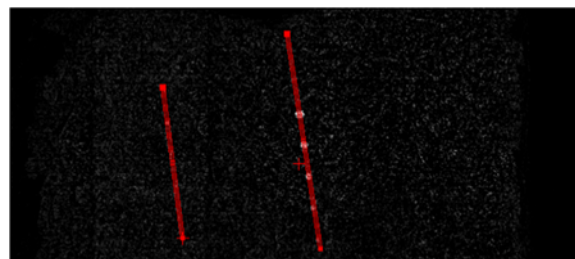


Fig. 8. Areal density image of aluminum with two line trackers of five pixels in width.

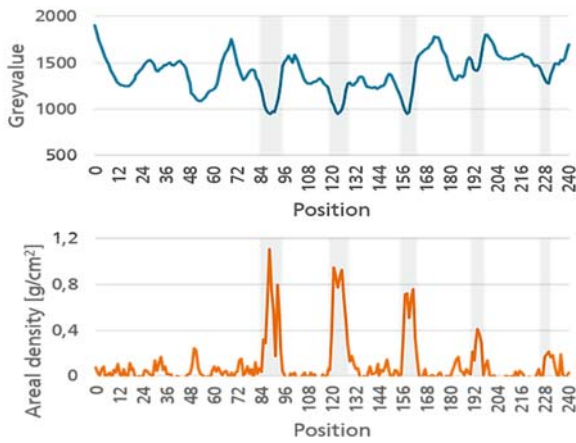


Fig. 9. Grey value in the HE X-ray projection (blue) and areal density (orange) of the five bigger test bodies (2.0 mm to 4.0 mm) acquired by a line tracker of five pixel in size. Grey pillars indicate the approximate positions of the five beads.

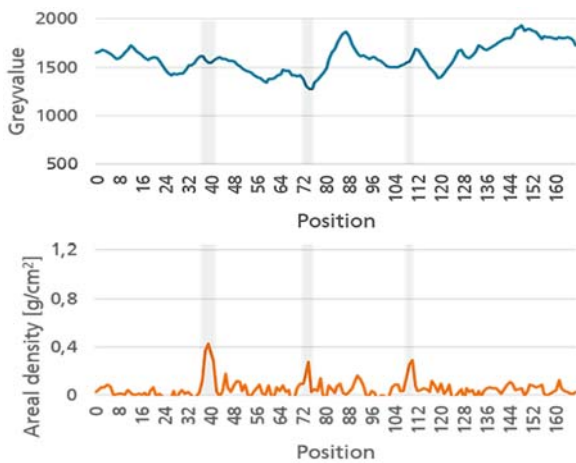


Fig. 10. Grey value in the HE X-ray projection (blue) and areal density (orange) of three of the five smaller test bodies (1.0, 1.2 and 1.5 mm) acquired by a line tracker of five pixel in size. Grey pillars indicate the approximate positions of the three beads.

Of the smaller set (Fig. 10), only the biggest test body with $d = 1.5$ mm could be discriminated using a simple threshold. This example illustrates that for edge cases the ability to detect contaminants may depend on their local surrounding. For instance, similar sized foreign bodies may be detected at one location, while at a different position a longer penetration length through the surrounding food can increase noise and thus prevent a detection. Especially for these edge cases, the situation could be improved by applying further image processing methods. Morphological operators like opening could be used to remove noise but retain the ‘clusters’ of bright pixels caused by the foreign bodies. Also the use of artificial intelligence for de-noising of images attracts more and more interest [17].

In Fig. 11 the high-energy XRT image of the frozen paella can be seen. The image is very

heterogeneous due to the rice and vegetable pieces. Big squared darker regions trace back to pieces of salmon, more round spots to pieces of chicken. The five bigger test objects of synthetic bone (6.0 mm to 10.0 mm) are visible, while the smaller ones (2.0 mm to 6.0 mm) are very difficult to see. In contrast, the cubes of synthetic bone can be seen easily in the areal density image (Fig. 12), because the ‘background’, i.e. the paella ($Z_{\text{eff}} = 7.5$), vanishes almost completely.

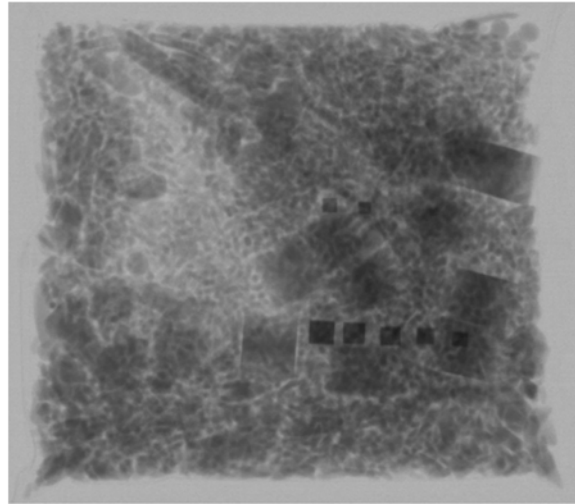


Fig. 11. High-energy XRT image of frozen paella contaminated with synthetic bones.

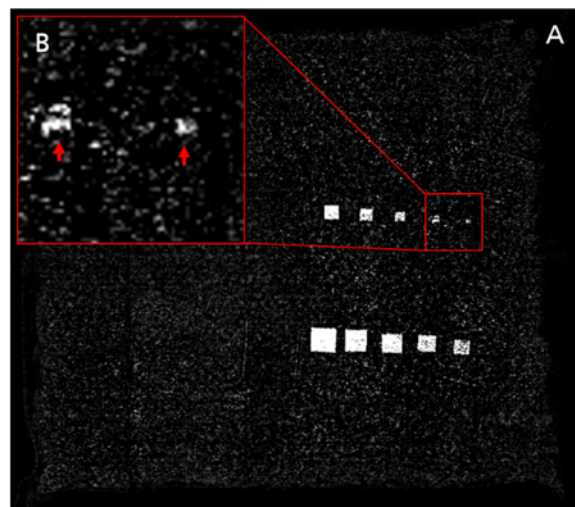


Fig. 12. A: Areal density image of (synthetic) bone. All ten contaminants are clearly visible. The frozen convenience food disappears. B: Magnification of 4 of the framed area in A (red). Red arrows indicate the approximate location of the synthetic bone cubes.

The strawberries in Fig. 13 are contaminated with glass beads. The images of three beads are overlapping the strawberries while two are placed (close) beside them. Due to the overlap, it is not possible to distinguish all the glass spheres from the food by thresholding.

In the BMD image (Fig. 14) this problem does not occur: all five bigger glass beads (1.5 mm to 3.5 mm) can be detected because the strawberries disappear ($Z_{\text{eff}} = 7.4$). The smaller beads (0.5 mm to 1.2 mm) of the second test card are beyond the detection limit. The biggest one of this set is equal in diameter to the smallest bead of the first test card ($d = 1.5$ mm). Nevertheless, it can not be detected as it is situated on top of a strawberry. In contrast, the equally sized bead in the first test card is not overlapping any fruit. Again, this shows the dependence of the detection limit for edge cases on the environment.

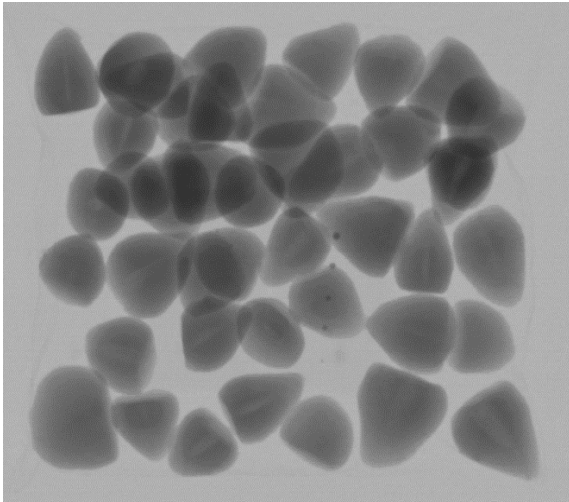


Fig. 13. High-energy XRT image of frozen strawberries contaminated with glass.

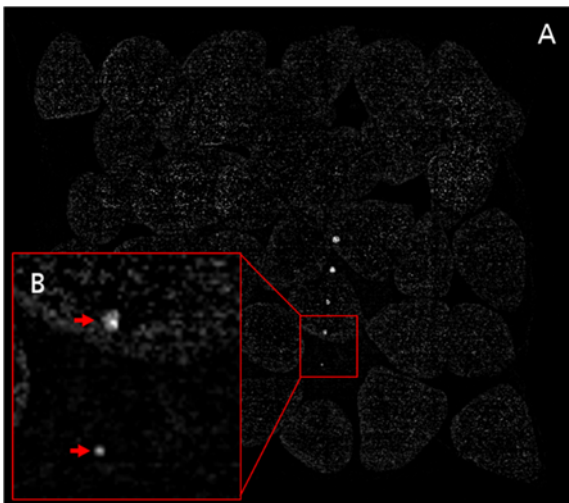


Fig. 14. A: Areal density image of glass. The five bigger contaminants are clearly visible. The frozen strawberries disappear. B: Magnification of 4 of the framed area in A (red). Red arrows indicate the approximate location of the glass beads.

In Fig. 15 the highly heterogeneous high-energy XRT image of frozen buttered vegetables can be seen. This sample is contaminated with steel test bodies with a diameter between 0.3 mm and 1.5 mm. Some of

them can be seen with the bare eye but despite the high contrast in the effective atomic numbers ($Z_{\text{eff}} = 7.2$ and $Z = 26$) only the three biggest ones can be detected easily by segmentation.

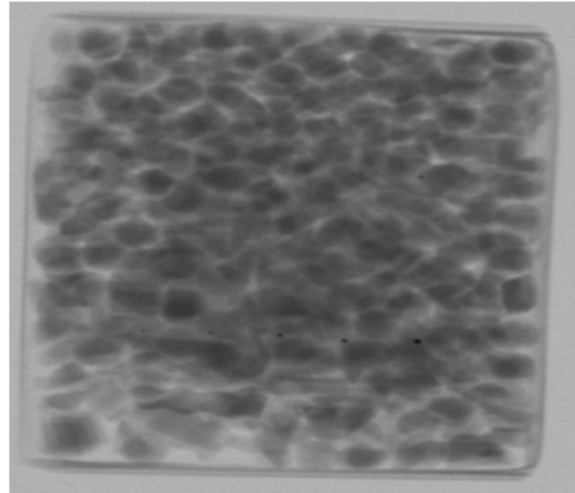


Fig. 15. High-energy XRT image of frozen buttered vegetables contaminated with steel AISI 304.

In the areal density image (Fig. 16), the steel contaminants can be seen much easier against the vanishing 'background'. While the four biggest spheres of the first test card (0.8 mm to 1.5 mm) can be detected easily by applying a threshold, the smallest one (0.6 mm) needs some image processing to be segmented.

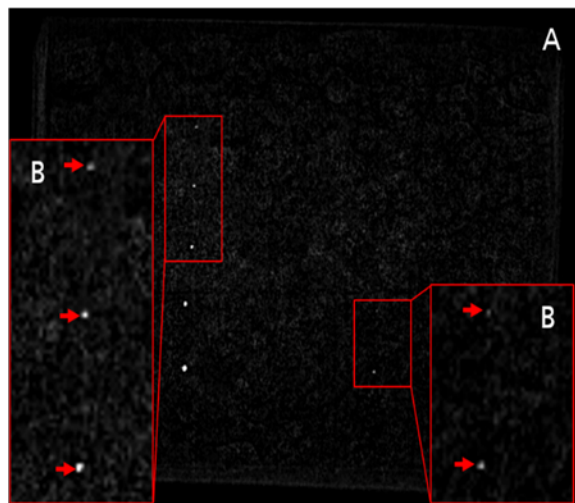


Fig. 16. A: Areal density image of steel. The four bigger contaminants are clearly visible. The smallest bead of the card with the bigger contaminants and the biggest bead of the card with the smaller contaminants are visible with some effort. The frozen vegetables disappear. B: Magnification of 2.5 of the framed areas in A (red). Red arrows indicate the approximate location of the steel beads.

The same is true for the biggest sphere of the second test card (0.8 mm). The second biggest bead of

this card is hardly visible with the bare eye and thus marks the detection limit. Again, the reason for the difference in detectability for equally sized beads in the two test cards is their different location on the sample.

Fig. 17 displays a high energy XRT image of a berry mix that has been contaminated with PTFE. The test objects can not be recognized based on their grey values. This is expected as their effective atomic number ($Z_{\text{eff}} = 10$) is very close to food ($Z_{\text{eff}} = 7.5$) due to their chemical composition (carbon and flour). Thus, they hardly increase the attenuation in comparison to food.

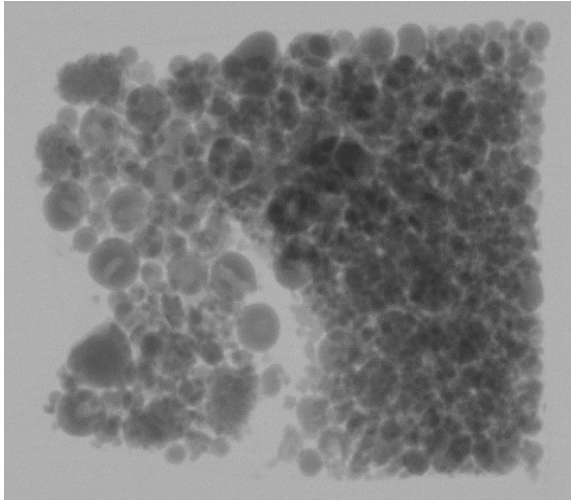


Fig. 17. High-energy XRT image of a frozen berry mix contaminated with PTFE.

The chemical similarity of PTFE and food also prevents the successful application of the BMD. In the areal density image shown in Fig. 18, the test objects can not be distinguished from noise. The two largest spheres ($d = 7$ mm and $d = 8$ mm) are visible only as a cluster of bright pixels with grey values similar to noise.

The line profiles in Fig. 19 show how low the contrast between the PTFE beads and their respective background is in both high-energy and areal density image.

4. Conclusion

Table 2 shows a summary of the results obtained for the various test specimen used as contaminants in the presented experiments. Their respective detectability is illustrated by different colors. Green means that a detection is possible by simply applying a threshold. Red indicates that finding the foreign body is not possible either because its size is below the spatial resolution limit of the detector and/or because its (effective) atomic number is too close to that of the food. Sizes labeled in yellow are edge cases. Here, thresholding is not sufficient to find the foreign bodies.

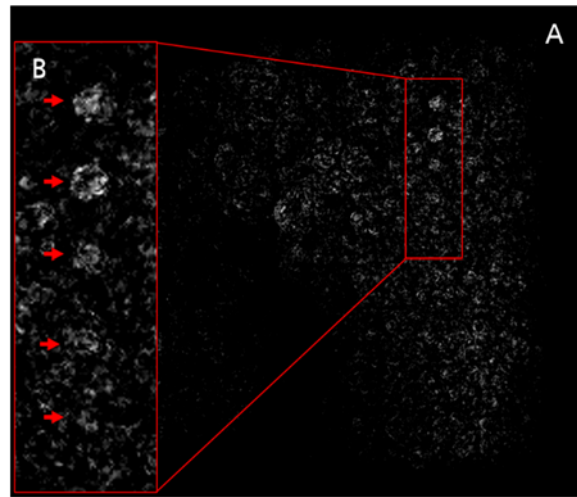


Fig. 18. A: Areal density image of PTFE. The contaminants are difficult to see. B: Magnification of 2.5 of the framed area in A (red). Red arrows indicate the approximate location of the PTFE beads.

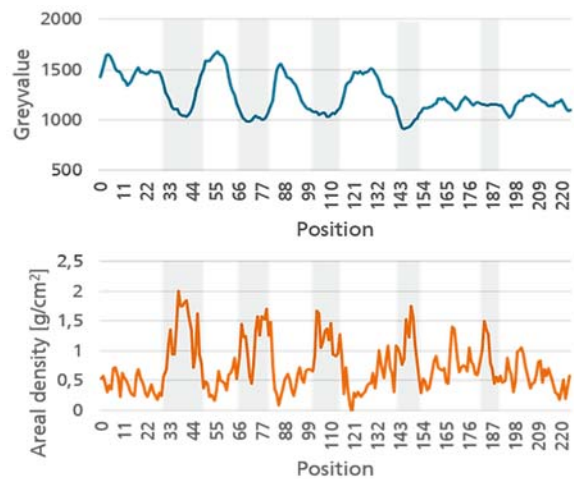


Fig. 19. Grey value in the HE X-ray projection (blue) and areal density (orange) of the five bigger test bodies (4.0 mm to 8.0 mm) acquired by a line tracker of five pixel in width. Grey pillars indicate the approximate positions of the five beads.

However, further image processing methods can allow their detection. Especially for foreign bodies with sizes marked in yellow, detectability may depend on the thickness of the food at their respective location.

The results of this study show that DE-XRT is a suitable and powerful method for detecting contaminants of various materials in frozen foods of different types. It can be shown that DE-XRT is able to detect aluminum, synthetic bone, glass and steel even in highly structured and heterogeneous environments like mixed berries or convenience food where standard XRT is likely to fail. The dual energy algorithm works the better, the more different the (effective) atomic numbers of the materials to be discriminated are. Thus, detecting PTFE in food was very difficult.

Table 2. Used test cards with their respective materials and thicknesses and their detectability for the presented approach and setup.

Material	Thickness [mm]				
	d ₁	d ₂	d ₃	d ₄	d ₅
Aluminum	0.5	0.8	1.0	1.2	1.5
Aluminum	2.0	2.5	3.0	3.5	4.0
Synth. Bone	2.0	3.0	4.0	5.0	6.0
Synth. Bone	6.0	7.0	8.0	9.0	10.0
Glass	0.5	0.8	1.0	1.2	1.5
Glass	1.5	2.0	2.5	3.0	3.5
Steel AISI304	0.3	0.4	0.5	0.6	0.8
Steel AISI304	0.6	0.8	1.0	1.2	1.5
Teflon PTFE	2.0	2.5	3.0	3.5	4.0
Teflon PTFE	4.0	5.0	6.0	7.0	8.0

	Detectable
	Detection Limit
	Not Possible

In general, the method is not only limited by the contrast in the atomic numbers, but also by the spatial resolution of the imaging system. For a reliable detection, contaminants have to be discriminated from the noise in the respective areal density images. Especially for contaminants with lower contrast to food, the size in the XRT images should preferably be at least 3 px x 3 px. This limits the detection of contaminants to sizes of $d \gtrsim 1.2$ mm, although a large difference in the atomic numbers might relax that criterion to some extent.

Acknowledgements

The authors would like to thank Hamamatsu Photonics Deutschland GmbH for providing the measurement setup at the Fraunhofer Development Center X-ray Technology in Fürth/ Germany.

References

- [1]. Website of Bundesamt für Arbeitsschutz und Arbeitsmedizin (<https://www.baua.de/DE/Angebote/Publikationen/Be-richte/ProdSG-2020.html>).
- [2]. Website of Food Safety Magazin (<https://www.food-safety.com/articles/2542-recall-the-food-industrys-biggest-threat-to-profitability?v=preview>).
- [3]. M. Graves, A. Smith, B. Batchelor, Approaches to foreign body detection in foods, *Food Science and Technology*, Vol. 9, Issue 1, 1998, pp. 21-27.
- [4]. R. P. Haff, N. Toyofuku, X-ray detection and contaminants in the food industry, *Sensing and Instrumentation for Food Quality and Safety*, Vol. 2, Issue 4, 2008, pp. 262-273.
- [5]. T. F. Schatzki, R. P. Haff, R. Young, I. Can, L.-C. Le, N. Toyofuku, Defect detection in apples by means of X-ray imaging, *Transactions of the American Society of Agricultural Engineers*, Vol. 40, Issue 5, 1997, pp. 1407-1415.
- [6]. R. P. Haff, D. C. Slaughter, Y. Sarig, A. Kader, X-ray assessment of translucency in pineapple, *Journal of Food Processing and Preservation*, Vol. 30, Issue 5, 2006, pp. 527-533.
- [7]. R. E. Alvarez, A. Macovski, Energy-selective reconstructions in X-ray computerised tomography, *Physics in Medicine and Biology*, Vol. 21, Issue 5, 1976, pp. 733-744.
- [8]. M. Firsching, J. Mühlbauer, A. Mäurer, F. Nachtrab, N. Uhlmann, Quantitative sorting using dual energy X-ray transmission imaging, in *Proceedings of the Conference on Optical Characterization of Materials (OCM'2013)*, Karlsruhe, Germany, 6-7 March 2013, pp. 259-264.
- [9]. M. Firsching, J. Lucic, A. Ennen, N. Uhlmann, Concentration determination for sorting applications using dual energy X-ray transmission imaging, in *Proceedings of the Conference on Optical Characterization of Materials (OCM'2017)*, Karlsruhe, Germany, 22-23 March 2017, pp. 65-74.
- [10]. C. Bauer, R. Wagner, J. Leisner, Potential of Dual Energy X-ray Transmission on Food Safety, in *Proceedings of the 7th International Conference on Sensors and Electronics Instrumentation Advances (SEIA'2021)*, Palma de Mallorca, Mallorca (Balearic Islands), Spain, 22-24 September 2021, pp. 90-93.
- [11]. Rondotest Website (<https://rondotest.de/>).
- [12]. C. Bauer, R. Wagner, B. Orberger, M. Firsching, A. Ennen, C. Garcia Pina, C. Wagner, M. Honarmand, G. Nabatian, I. Monsef, Potential of Dual and Multi Energy XRT and CT Analyses on Iron Formations, *Sensors*, Vol. 21, Issue 7, 2021, pp. 2455.
- [13]. M. Firsching, F. Nachtrab, N. Uhlmann, R. Hanke, Multi-Energy X-ray Imaging as a Quantitative Method for Materials Characterization, *Advanced Materials*, Vol. 23, Issue 22-23, 2011, pp. 2655-2656.
- [14]. M. Firsching, J. Mühlbauer, F. Nachtrab, A. Jobst, Basis Material Decomposition – a Quantitative X-ray Imaging Method and its Application in Industrial Sorting, in *Proceedings of the Symposium on Digital Industrial Radiology and Computed Tomography (DIR'2021)*, Berlin, Germany, 20-22 June 2011.
- [15]. E. Y. Sidky, L. Yu, X. Pan, Y. Zou, M. Vannier, A robust method of X-ray source spectrum estimation from transmission measurements: Demonstrated in computer simulated, scatter-free transmission data, *Journal of Applied Physics*, Vol. 97, Issue 12, 2005, pp. 124701-1 – 124701-11.
- [16]. B. Heismann, J. Leppert, K. Stierstorfer, Density and atomic number measurements with spectral X-ray attenuation method, *Journal of Applied Physics*, Vol. 94, Issue 3, 2003, pp. 2073-2079.
- [17]. A. E. Ilesanmi, T. O. Ilesanmi, Methods for image denoising using convolutional neural network: a review, *Complex & Intelligent Systems*, 2021, pp. 1-20.

